X-ray-boosted photoionization for the measurement of an intense laser pulse*

Ge Yu-Cheng(葛愉成)† and He Hai-Ping(何海萍)

School of Physics and State Key Laboratory of Nuclear Physics and Technology, Peking University, Beijing 100871, *China*

(Received 14 October 2012; revised manuscript received 21 January 2013)

Investigations show that X-ray-boosted photoionization (XBP) has the following advantages for *in-situ* measurements of ultrahigh laser intensity I and field envelope $F(t)$ (time t, pulse duration τ_L, carrier-envelope-phase Φ): accuracy, dynamic range, and rapidness. The calculated XBP spectra resemble inversely proportional functions of the photoelectron momentum shift. The maximum momentum $\boldsymbol{p}$ and the observable value Q (defined as a double integration of a normalized photoelectron energy spectrum, PES) linearly depend on $I^{1/2}$ and τ_L, respectively. Φ and $F(t)$ can be determined from the PES cut-off energy and peak positions. The measurable laser intensity can be up to and over 10^{18} W/cm^2 by using high energy X-rays and highly charged inert gases.

Keywords: measurement of ultrahigh laser pulse, X-ray-boosted photoionization, photoelectron energy spectrum, quantum interference

PACS: 32.80.Rm, 42.50.Hz, 42.65.Re **DOI:** 10.1088/1674-1056/22/6/063201

1. Introduction

In modern sciences and technologies, the laser occupies an important position, and the strong field physics is one of the scientific frontiers. Recent advances in laser technology have made it possible to obtain single optical cycle pulses.[1] A table-top laser system or a large facility can produce intensities in excess of 10^{18} W/cm^2 or up to 10^{22} W/cm^2.[2] Thus far, ultrashort and ultrahigh lasers have been used as pump/probe pulses in above-threshold ionization (ATI),[3] high-order harmonic generation,[4] nonlinear Compton scattering,[5] and laser acceleration.[6] To either produce or use ultrahigh laser pulses, it is critical to know the peak intensity I, the field envelope $F(t)$, and the carrier-envelope phase (CEP) Φ of each pulse; however, measuring these parameters in real time is challenging. This can be attributed to (i) a lack of nonlinear optical effects that can be used in measurements with broad intensity dynamic ranges, and (ii) few detectors can survive in ultrahigh fields without damage.

Ultrahigh laser intensities are usually estimated from the focal spot size, the energy in the spot, and the temporal profile of the pulse, which are typically measured using an autocorrelation method. The estimation is subject to many errors that quickly add up to about 50% uncertainty in the intensity[7] or to a value even several times higher than the actual intensity. More recently proposed measurement techniques include measuring the field ionization of highly charged inert gases (I around 10^{20} W/cm^2),[8,9] Thomson scattering from single and multiple electrons ($I \geq 10^{18}$ W/cm^2), and the momentum transferred to the photo-ion and photoelectron.[10,11]

Studies have shown that a few-cycle ultrahigh laser leaves a clear fingerprint on a photoelectron energy spectrum (PES) as it passes through a gas involving X-ray radiation. The spectrum exhibits interesting energetic and statistical properties due to the field modulation and strong quantum interference between the photoelectron wave packets. The spectral energetic width and the total X-ray photoionization sensitively reflect the laser field strength and the pulse duration, respectively. The linear relations between these spectral values and the laser parameters (intensity, carrier-envelope phase, pulse-duration) suggest new methods for ultrahigh-laser-pulse measurement *in-situ*. Calculations show that these methods can be used to measure laser intensities up to 10^{16} W/cm^2 with sub-keV X-rays, or intensities up to 10^{18} W/cm^2 by using higher energy X-rays and highly charged inert gases.

Different from the other ionization methods that have very limited dynamic measurement ranges (e.g., several times of the intensity),[8,9] the proposed methods have advantages of accuracy, simplicity, speed, and large dynamic ranges (up to many orders of intensity). Furthermore, all pulse information including the laser intensity, field envelope, and carrier-envelope phase can be directly determined from the energetic and statistical properties of a measured PES without any time-resolved measurements and data iterating and fitting processes. Different from the conventional streaking methods[12–15] (including our previous research works[16–22]) for the measurements of attosecond X-ray pulses by using intense few-cycle lasers (whose parameters must be measured in advance), the new configuration for the measurement of ultrahigh laser pulses by using narrowband continuous X-rays (or X-ray pulses whose durations are much longer than the laser)

*Project supported by the National Natural Science Foundation of China (Grant No. 11175010).

†Corresponding author. E-mail: gyc@pku.edu.cn

© 2013 Chinese Physical Society and IOP Publishing Ltd

has different purposes, different physical results (spectral patterns), and different data analysis algorithms. The attosecond streaking measurements involve time-resolved measurements and data iterating and fitting procedures.[23–27]

In this paper, we report some theoretical results of the X-ray-boosted photoionization (XBP) under the new configuration for *in-situ* measurements of ultrahigh laser pulses. The methods are based on the analysis of the XBP spectral energetic and statistical properties. The PES are calculated using strong field approximation (SFA).[28]

The paper is organized in sections. Section 2 is dedicated to an introduction of the SFA theory[28] and the stationary point method[16–22] for calculations of the XBP PES and the classically predicted spectral values. Section 3 shows some ATI data calculated in the absence of the X-ray for comparison with the XBP. Section 4 is divided into three subsections. In Subsection 4.1, the XBP PES calculated with different laser parameters are investigated. In Subsection 4.2, the XBP energetic properties including the spectral cut-off energies are closely examined. In Subsection 4.3, the XBP statistical properties including the total XBP photoionization yield and the double integration of the XBP PES is analyzed. Section 5 concludes our findings.

2. Strong field approximation

For a cross-correlation between a laser pulse and a narrowband continuous X-ray (or an X-ray pulse that is much longer than the laser), both were synchronized and collinearly propagating in Z direction (called 0°-correlation), the generated PES can be calculated from the probability amplitude for transitioning from the ground state $|0\rangle$ to a final momentum ($\boldsymbol{p}$) state $|\boldsymbol{p}\rangle$,[28]

$$b(\boldsymbol{p}) = \mathrm{i}\int_{-\infty}^{\infty} \mathrm{d}t\, \boldsymbol{E}(t)\cdot\boldsymbol{d}[\boldsymbol{p}-\boldsymbol{A}(t)]\,\mathrm{e}^{-\mathrm{i}\widetilde{S}(t)}, \tag{1}$$

where $\widetilde{S}(t)$ is the quasi-classical action,

$$\widetilde{S}(t) = \int_{t}^{\infty} \mathrm{d}t'[\boldsymbol{p}-\boldsymbol{A}(t')]^2/2 + I_{\mathrm{p}}t. \tag{2}$$

$\boldsymbol{E}(t)$ and $\boldsymbol{A}(t)$ describe the combined electric fields and vector potentials of the linearly polarized laser and the X-ray with amplitudes $E_L(t)$ and $E_X(t)$ ($\equiv E_X$, a constant value), respectively. ω_L and ω_X are the angular frequencies of the laser and X-ray, respectively. Φ is the CEP of the laser. t denotes time and $E(t) = E_L(t)\cos(\omega_L t+\Phi) + E_X\cos(\omega_X t)$ (X direction). I_{p} is the atomic ionization potential. $\boldsymbol{d}(\boldsymbol{p}) = \langle\boldsymbol{p}|\boldsymbol{x}|0\rangle$ denotes the atomic dipole matrix element for the bound-free transition, and $d_x(\boldsymbol{p})$ is the component parallel to the polarization axis (X direction). The above discussion is also applied to the 90°-correlation measurement where the X-ray propagates in the Y direction, as shown in Fig. 1(a) (color online). Obviously, $b(\boldsymbol{p})$ describes the quantum interference between the electron wave packets that are generated at different times, and each photoelectron carries the information of the whole laser pulse. In the following, atomic units and model atoms (e.g., hydrogen-like atoms) are used for simplicity [$I_{\mathrm{p}} = 13.6$ eV, $d_x(\boldsymbol{p}) = \mathrm{i}2^{19/4}I_{\mathrm{p}}^{5/4}\boldsymbol{p}/\pi(2I_{\mathrm{p}}+\boldsymbol{p}^2)^3$ for s state]. The laser intensities used in quantum mechanical calculations by applying SFA are selected on the model assumptions that (I) the laser intensities I are below the saturation ionization level I_{sat}, assuring no ground state depletion, and (II) the Keldish parameter $\gamma = \sqrt{I_{\mathrm{p}}/2U_{\mathrm{p}}} < 1$, where U_{p} is the ponderomotive energy, $U_{\mathrm{p}} = I/2\omega_L^2$.

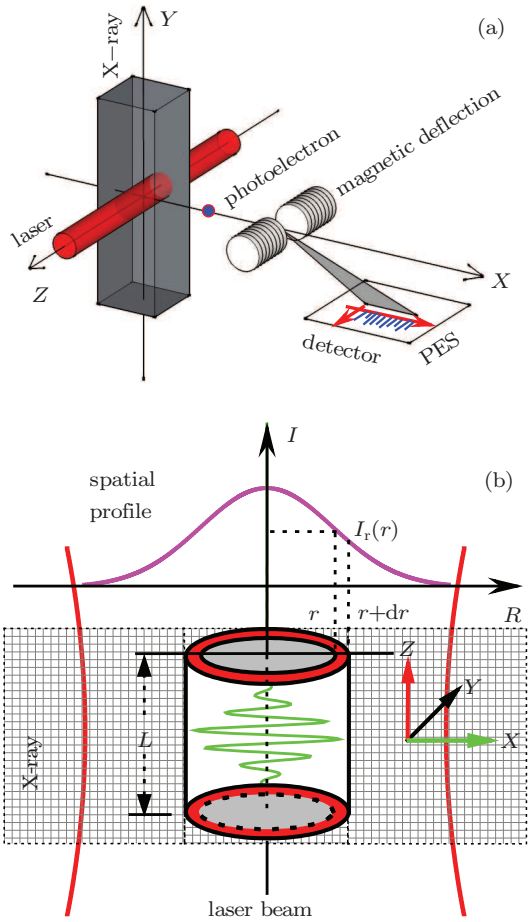


Fig. 1. (color online) XBP configuration. (a) Illustration of the cross-correlation between an X-ray and a laser pulse. The X-ray can be filtered from the high harmonic radiation or the synchrotron radiation. A photoelectron that flies out from the interactive region is deflected by a magnetic field and collected by a spectrometer. Photoelectrons with specific energies of interest are selected by adjusting the magnetic field. (b) A spatial profile of the laser intensity, $I_{\mathrm{r}}(r) = \exp[-4\ln 2(r)^2/\tau_R^2]$ (magenta line), and an iso-intensity shell in the interaction volume (radius r, length L, thickness $\mathrm{d}r$).

Physically, $|b(\boldsymbol{p})|^2$ is the photoelectron momentum spectrum $n(\boldsymbol{p})$, and its conversion to the PES is $n(W) = |b(\boldsymbol{p})|^2/\sqrt{2W}$, where W is the photoelectron energy. $b(\boldsymbol{p})$ can be expressed as $b(\boldsymbol{p}) = b_1(\boldsymbol{p}) + \varepsilon$, where

$$b_1(\boldsymbol{p}) = \frac{1}{2}\mathrm{i}\int_{-\infty}^{\infty} \mathrm{d}t E_X d_x[\boldsymbol{p}-\boldsymbol{A}(t)]\,\mathrm{e}^{-\mathrm{i}\widetilde{S}_1(t)} \tag{3}$$

is a dominant term that is contributed by the X-ray and ε is the residual including the laser contribution. Here,

$$\widetilde{S}_1(t) = \int_t^{\infty} \mathrm{d}t' \frac{[\boldsymbol{p} - \boldsymbol{A}(t')]^2}{2} + (\omega_X - I_\mathrm{p})t \tag{4}$$

is the quasi-classical action of $b_1(\boldsymbol{p})$. In the time domain, $\widetilde{S}_1(t)$ has many stationary points $(\boldsymbol{p}_{\mathrm{st},j}, t_{\mathrm{st},j})$ $(j = 1, 2, \ldots)$ for each momentum $\boldsymbol{p}$, where

$$\left.\frac{\mathrm{d}\widetilde{S}_{1,j}(t)}{\mathrm{d}t}\right|_{t=t_{\mathrm{st},j}} = \frac{[\boldsymbol{p}_{\mathrm{st},j} - \boldsymbol{A}_L(t_{\mathrm{st},j})]^2}{2} - (\omega_X - I_\mathrm{p}) \equiv 0. \tag{5}$$

Equation (5) is the stationary point equation, which gives the initial kinetic energy of the generated electron $W_0 = \boldsymbol{v}_{i,j}^2/2 = [\boldsymbol{p}_{\mathrm{st},j} - \boldsymbol{A}_L(t_{\mathrm{st},j})]^2/2 \equiv \omega_X - I_\mathrm{p}$. At time $t = t_{\mathrm{st},j} + \Delta t$ (Δt is a small value),

$$\widetilde{S}_1(t) = \widetilde{S}_1(t_{\mathrm{st},j}) + \frac{1}{2}\left.\frac{\partial^2 \widetilde{S}_1(t)}{\partial t^2}\right|_{t=t_{\mathrm{st},j}} (t - t_{\mathrm{st},j})^2 \tag{6}$$

is a good approximation, and the transition probability amplitude is

$$\begin{aligned} &\Delta b_1(\boldsymbol{p}_{\mathrm{st},j}, t_{\mathrm{st},j}, \Delta t) \\ &= \frac{1}{2}\mathrm{i}\int_{t_{\mathrm{st},j}}^{t_{\mathrm{st},j}+\Delta t} \mathrm{d}t E_X d_x[\boldsymbol{p}_{\mathrm{st},j} - \boldsymbol{A}(t)]\,\mathrm{e}^{-\mathrm{i}\widetilde{S}_1(t)} \\ &= \frac{1}{2}\mathrm{i}\Delta t E_X d_x[\boldsymbol{p}_{\mathrm{st},j} - \boldsymbol{A}(t_{\mathrm{st},j})]\,\mathrm{e}^{-\mathrm{i}\widetilde{S}_1(t_{\mathrm{st},j})}. \end{aligned} \tag{7}$$

We define $b_1(\boldsymbol{p}_{\mathrm{st}}, t_{\mathrm{st}}) \equiv \sum_j \Delta b_1(\boldsymbol{p}_{\mathrm{st},j}, t_{\mathrm{st},j}, \Delta t)/\Delta t$ as the semi-classical prediction of $b(\boldsymbol{p})$:

$$b_1(\boldsymbol{p}_{\mathrm{st}}, t_{\mathrm{st}}) = \sum_j \frac{1}{2}\mathrm{i}E_X d_x[\boldsymbol{p}_{\mathrm{st},j} - \boldsymbol{A}(t_{\mathrm{st},j})]\,\mathrm{e}^{-\mathrm{i}\widetilde{S}_1(t_{\mathrm{st},j})}. \tag{8}$$

The semi-classical prediction of the PES is $n_{\mathrm{sc}}(W) \equiv |b_1(\boldsymbol{p}_{\mathrm{st}}, t_{\mathrm{st}})|^2/\sqrt{2W}$. In the following calculations,

$$F(t) = \exp[-4\ln 2(t)^2/\tau_L^2] \tag{9}$$

is a Gaussian-like time function of the laser field envelope with a full width at half maximum (FWHM) pulse duration τ_L. The laser intensity profile is $I(t) = I_0 F^2(t)$, where $I_0 \equiv I = \frac{1}{2}E_L^2$ is the laser peak intensity. To compare $n_{\mathrm{sc}}(W)$ to the $n(W)$ of PES, $n(W)$ is divided by the square of the pulse area, ΔT^2, where $\Delta T = \int_{-\infty}^{+\infty} F^2(t)\mathrm{d}t$. In discussing the total XBP photoionization production or yield, we must consider the spatial profile of the laser intensity. A Gaussian-like spatial profile,

$$I_\mathrm{r}(r) = \exp[-4\ln 2(r)^2/\tau_R^2] \tag{10}$$

is used, where r is the radial variable of the laser beam, and τ_R is the FWHM radius, as shown in Fig. 1(b).

3. Above-threshold ionization

Before discussing XBP, we calculate the ATI spectra (in the absence of the X-ray, $E_X = 0$) by applying SFA for comparison. Figure 2(a) shows the ATI spectra $n(W)$ calculated with the laser wave length $\lambda_L = 750$ nm, pulse duration $\tau_L = 7$ fs, CEP $\Phi = 0°$, observation angle $\theta = 0°$, and different laser intensities I. Here, θ is defined as the angle between the electron momentum $\boldsymbol{p}$ and the laser-field polarization. The filled circles in Figs. 2(b) and 2(c) depict the ionization productions $Y_L = \int n(W)\mathrm{d}W$ (in arbitrary units) calculated with different laser intensities I (for $\tau_L = 7$ fs) and different laser pulse durations τ_L (for $I = 5 \times 10^{14}$ W/cm^2), respectively. The open circles in Figs. 2(b) and 2(c) depict the ionization productions for $W > 15$ eV, i.e., $Y_{L>15\ \mathrm{eV}} = \int_{15\ \mathrm{eV}} n(W)\mathrm{d}W$. The solid line in Fig. 2(b) is a polynomial fit of the data, $Y_{L>15\ \mathrm{eV}} = \sum_{k=1}^{5} a_k I^k$ (I has the units of 10^{12} W/cm^2). The solid line in Fig. 2(c) is a linear fit of the data, $Y_{L>15\ \mathrm{eV}} = -0.0035 + 0.0039\tau_L$ (τ_L has the units of fs). The filled circles and solid line in Fig. 2(d) plot the spectral cut-off energies W_{cut} at different I ($\tau_L = 7$ fs) and a linear fit of the data, respectively. The dotted line plots the classical predictions of the spectral cut-off energies, $W_{\mathrm{cl.cut}} = 3.17U_\mathrm{p}$.

From Figs. 2(b) and 2(c), we see that $Y_{L>15\ \mathrm{eV}}$ continuously increases as I or τ_L increases. Considering the spatial distribution of the laser intensity, as shown in Fig. 1(b), the number of the photoelectrons generated in an iso-intensity shell (radius r, thickness $\mathrm{d}r$, length L) and moving in $\theta = 0°$ direction is

$$\mathrm{d}Y = g\eta\rho \cdot 2\pi r \mathrm{d}r L \cdot \sum_{k=1}^{5} a_k I^k I_\mathrm{r}^k(r), \tag{11}$$

where g is the geometric factor, η is the detection efficiency, and ρ is the atomic density. The total ATI production [$W >$ 15 eV, $\tau_L = 7$ fs, Fig. 2(b)] is

$$Y_{\mathrm{ATI}} = \int \mathrm{d}Y = \sum_{k=1}^{5} A_k I^k, \tag{12}$$

where

$$A_k = 2\pi g\eta\rho L a_k \int_0^{\infty} \mathrm{d}r \cdot r\,\mathrm{e}^{-4\ln 2 \cdot r^{2k}/\tau_R^2} \tag{13}$$

are constant values associating with the mathematical productions of a_k ($k = 1, 2, \ldots, 5$) and constant spatial integrations $\int_0^{\infty} \mathrm{d}r \cdot r\,\mathrm{e}^{-4\ln 2 \cdot r^{2k}/\tau_R^2}$. Because i) the ATI production $Y_{L>15\ \mathrm{eV}}$ linearly depends on the pulse duration τ_L for a specified laser intensity I, i.e., factors a_k of the polynomial fit can be substituted by a value of ξa_k where ξ is a constant value for different pulse durations and different k numbers, and ii) the spatial integrations $\int_0^{\infty} \mathrm{d}r \cdot r\,\mathrm{e}^{-4\ln 2 \cdot r^{2k}/\tau_R^2}$ ($k = 1, 2, \ldots, 5$) are the same for different pulse durations, thus the linear fit line in Fig. 2(c) can be modified to another linear line Y_{ATI} versus τ_L

[or $Y_{\rm ATI}(\tau_L)$] for the volume integration of the ATI productions. Experimentally, the laser intensity I can be directly read from the linear line of the spectral cut-off energy $W_{\rm cut}$ versus I [Fig. 2(d)]. A calculated (or measured) line $Y_{\rm ATI}(\tau_L)$, which is calibrated with known τ_L pulses, can be used for the τ_L measurement; however, $Y_{\rm ATI}(I)$ increases by 1.2 as I changes from 1.3×10^{14} W/cm^2 to 1.75×10^{15} W/cm^2, and $Y_{\rm ATI}(\tau_L)$ increases by 0.22 as τ_L changes from 5 fs to 60 fs. These small increases of $Y_{\rm ATI}(I)$ and $Y_{\rm ATI}(\tau_L)$ over these intensities and pulse durations have limited the sensitivity and the measurable ranges of I and τ_L, leading us to seek more effective ways for the measurement of ultrahigh laser pulses.

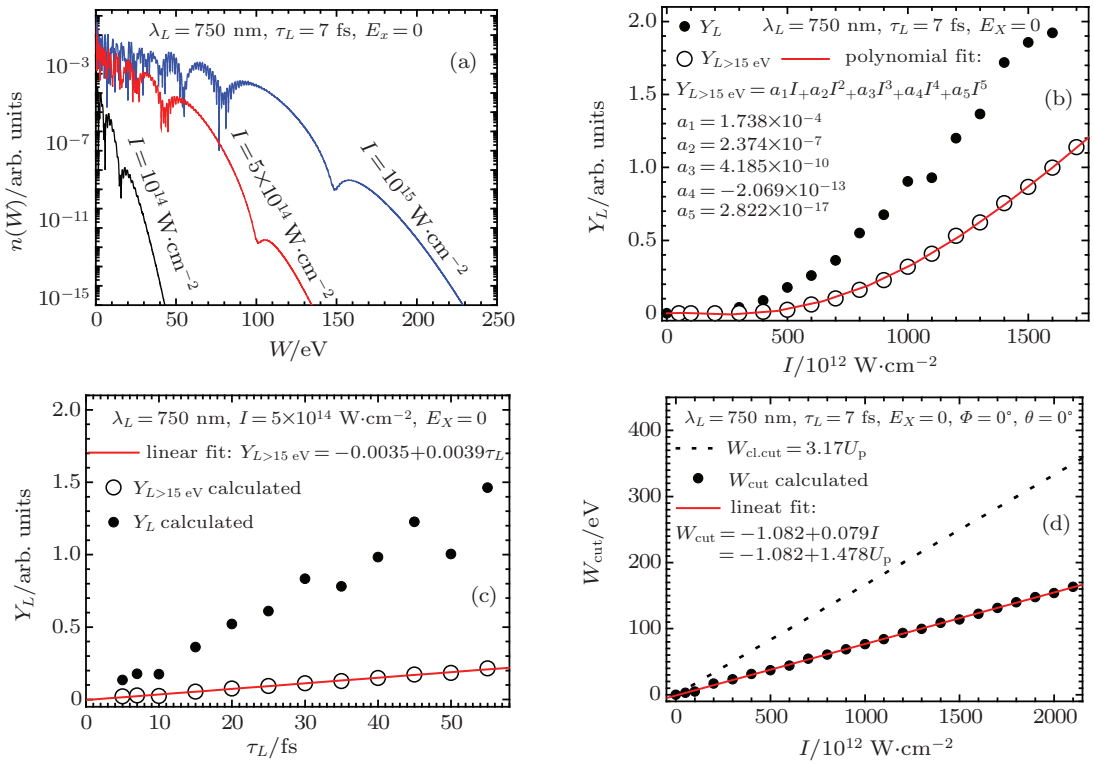


Fig. 2. (color online) ATI spectra calculated with SFA. (a) ATI spectra $n(W)$ calculated with $E_X=0$, $\lambda_L=750$ nm, $\tau_L=7$ fs, $\theta=0°$, and different I varying from 10^{14} W/cm^2 to 1.5×10^{15} W/cm^2. (b) ATI production Y_L versus I ($\tau_L=7$ fs). Filled circles: $Y_L=\int n(W)\,{\rm d}W$; open circles: $Y_{L>15\ {\rm eV}}=\int_{15\ {\rm eV}} n(W)\,{\rm d}W$; solid line: a polynomial fit of the data. (c) Y_L versus τ_L ($I=5\times10^{14}$ W/cm^2). Filled circles: $Y_L=\int n(W)\,{\rm d}W$; open circles: $Y_{L>15\ {\rm eV}}=\int_{15\ {\rm eV}} n(W)\,{\rm d}W$; solid line: a linear fit of the data. (d) ATI cut-off energy $W_{\rm cut}$ versus I ($\tau_L=7$ fs). Filled circles: $W_{\rm cut}$; solid line: a linear fit of the data; dotted line: the classical predictions of the spectral cut-off energies $W_{\rm cl.cut}=3.17U_{\rm p}$.

4. X-ray-boosted photoionization

Besides the low sensitivity of the total ATI production $Y_{\rm ATI}$ to the laser intensity and pulse duration, Fig. 2(a) also shows that a) the ATI spectra are lacking structures associated with the temporal structure of the electric field of the laser pulse, and b) the spectral values are less than 10^{-27} at higher energies (e.g. $W>300$ eV), i.e., the ATI electrons at these energies are not measurable. As discussed in the following, the spectral values of the XBP at higher energies are much higher than those of the ATI. The XBP spectra are measurable and they have interesting structures from which all information of the laser pulse can be derived.

4.1. XBP PES

Figure 3(a) shows an XBP PES, $n(W)$, calculated with time t ranging from -35 fs to $+35$ fs, $\lambda_L=750$ nm, $\tau_L=7$ fs, $\Phi=0°$, $I=10^{15}$ W/cm^2, $\theta=0°$, $\omega_X=1$ keV, and energy step sizes of 0.02 eV. Here, the X-ray intensity I_X is set to a value of 5.41×10^8 W/cm^2 without any specific consideration because $n(W)$ is proportional to I_X. The red line in Fig. 3(a) plots the laser-induced contribution $n_L(W)$ for comparison. The spectra clearly show two measurable portions: one is that $W<W_L=251$ eV, which is mainly derived from the laser field (ATI), and another is 457 eV $<W<$ 1734 eV, which is mainly derived from $b_1(\boldsymbol{p})$ (XBP PES). The lower and upper cut-off energies are denoted as $W_{\rm a}$ and $W_{\rm b}$, respectively. Obviously, $n(W)$ is significantly enhanced by the ATI spectrum because of the X-ray at $W>W_L$. The black, magenta, and green lines plot $n_q(W)=n(W)/\Delta T^2$ (including the full interference between all of the electrons), the semi-classical prediction $n_{\rm sc}(W)$ (interference between electrons generated at the stationary points), and the classical prediction $n_{\rm c}(W)$

[without interference, which is shifted to a blue line by multiplying $n_c(W)$ with a factor of 10^6 for clarity], respectively. These spectra show that the interference behaves in a way of strong destruction, and the classical predictions represent the averaged values of the quantum results. The red oscillating line in the inset of Fig. 3(b) depicts

$$W(t) = W_0 + 2U_p F^2(t)\sin^2(\omega_L t + \Phi) + \sqrt{8U_p W_0}F(t)\sin(\omega_L t + \Phi), \quad (14)$$

where $W(t)$ is the final energy of a photoelectron generated at $t = t_{st}$ and moving at $\theta = 0°$. The corresponding momentum is

$$p(t) = p_0 + 2\sqrt{U_p}F(t)\sin(\omega_L t + \Phi), \quad (15)$$

where $p_0 = \sqrt{2W_0}$. The relatively higher peak positions of $n(W)$ and $n_c(W)$ correspond to the times when the vector potential $A(t)$ of the laser field reaches different extremes.

Figure 3(c) (in linear scales) shows an expanded area of Fig. 3(a), corresponding to the X-ray-boosted photoionizations. We see that the XBP spectrum has peak groups, each includes small peaks. Figure 3(c) also shows some spectral symmetry by W_0. The complicated XBP spectral structures indicate very strong quantum interference between photoelectron wave packets generated at different times. From Figs. 3(b) and 3(c), we see that the data of the peak positions of the XBP PES consist of a fingerprint of the laser field envelope $F(t)$.

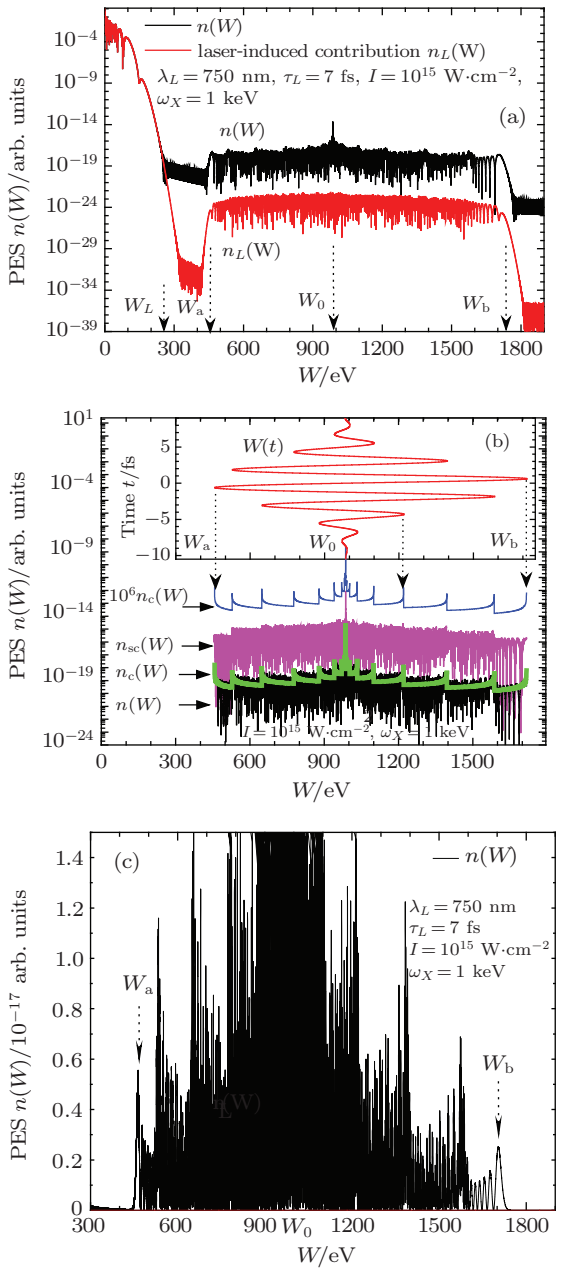


Fig. 3. (color online) XBP PES. (a) Black line: $n(W) = |b(p)|^2/\sqrt{2W}$; red line: the laser-induced contribution. (b) Black line: $n_q(W) = n(W)/\Delta T^2$; magenta line: the semi-classical prediction $n_{sc}(W)$; green line: the classical prediction $n_c(W)$ [shifted to a blue one, $10^6 n_c(W)$]. The red line in the inset depicts the final energy $W(t)$ of a photoelectron born at the stationary point t and moving at $\theta = 0°$ ($\Phi = 0°$). (c) An expanded area of (a), corresponding to the X-ray-boosted photoionizations.

4.2. XBP energetic properties

To closely examine the XBP PES, we plot $p(t)$ in Fig. 4(a) (an oscillating line partly highlighted for a laser optical cycle, T; $\theta = 0°$; $\Phi = 0°$), $n(p) = |b(p)|^2$ (a violet line), and its smoothed one, $n_s(p)$ (a red line, adjacently averaged in 4 eV). From the classical point of view, the photoelectrons generated in an optical cycle (T) are populated between momentums $p_0 - 2\sqrt{U_p}F(t)$ and $p_0 + 2\sqrt{U_p}F(t)$ [length $L_p = 4\sqrt{U_p}F(t)$]. At a turning point of $p(t)$, a time interval T corresponds to a momentum interval dp of the spectrum. If the ionization rate by X-ray is σ and the photoelectron population is uniform, the contribution to the momentum spectrum $n(p)$ is $dN \approx \sigma T \cdot dp/L_p$. Thus, $n_1(p) \approx 2dN/dp = \sigma T/|p - p_0|$. Here, the contributions from other optical cycles are neglected, whereas those from time $-t$ in an interval T are included. $n_1(p)$ is an inverse proportion function of $|p - p_0|$. The actual shape of a measured $n(p)$ may be close to $n_\mu(p) = \mu n_1(p) = \mu\sigma T/|p - p_0|$, where μ is a proportional factor. The colored lines in Fig. 4(b) are the smoothed spectra $n_s(p)$ calculated with different I and τ_L. Each one has a symmetrical pattern between the lower and upper cut-off momentums p_a and p_b. Calculations indicate that p_a (p_b) depends on I and Φ but not on τ_L. $n(p)$ for $\tau_L = 7$ fs (55 fs) is valued between $n_{0.25}(p)$ and $n_{2.5}(p)$ [$n_6(p)$ and $n_9(p)$]. The filled and open circles in Fig. 4(c) plot the W_b values at different Φ. If $n_s(p)$ is peaked at p_b ($\equiv p_1$), p_j ($j = 2, 3, \ldots, p_j > p_{j+1} > p_0$), the field envelopes $F(t)$ and Φ satisfy $F(t = [(2j-1)\pi - \Phi]/\omega_L) = (p_j - p_0)/2\sqrt{U_p}$. The filled circles in Fig. 4(d) plot $W_b^{1/2}$ values that have been calculated with different I. The solid line is a linear fit of $W_b^{1/2}$ data. This line can be used to determine I from $W_b^{1/2}$.

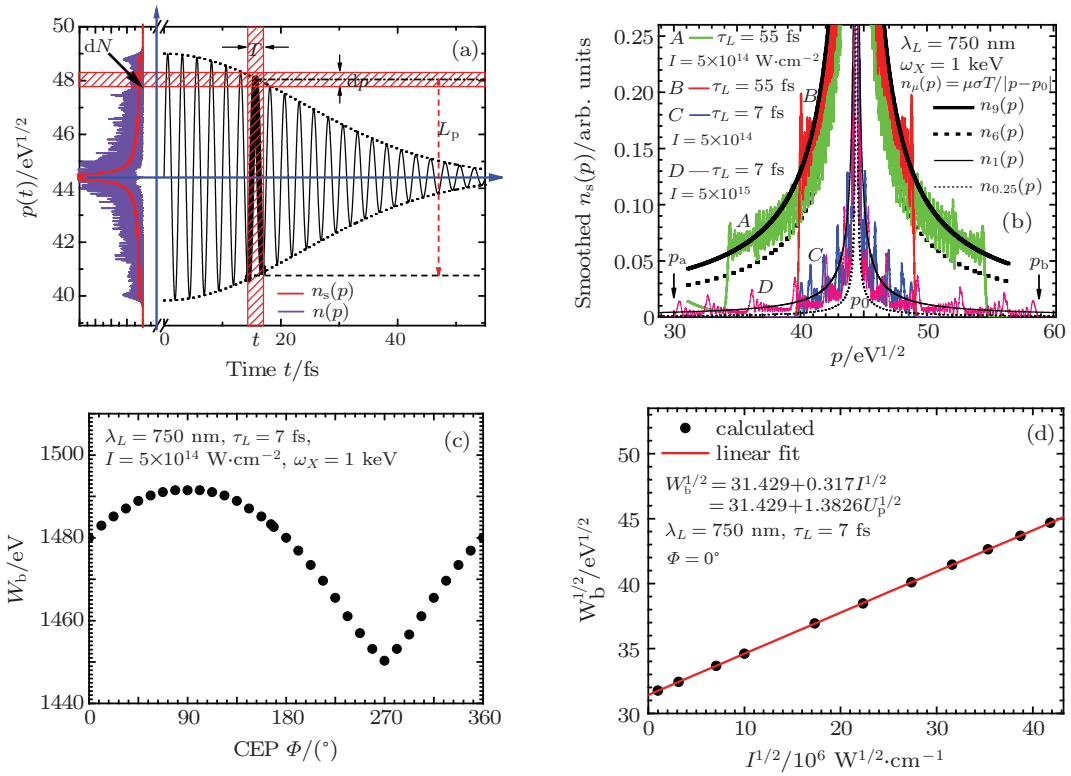


Fig. 4. (color online) XBP energetic properties. (a) Analysis of an XBP spectrum. Black solid line: the final photoelectron momentum $\boldsymbol{p}(t)$; highlighted curve: $\boldsymbol{p}(t)$ in a laser optical cycle T; violet line: $n(\boldsymbol{p}) = |b(\boldsymbol{p})|^2$; red line: $n_s(\boldsymbol{p})$ smoothed from $n(\boldsymbol{p})$. (b) Colored lines: $n_s(\boldsymbol{p})$ calculated with different I and τ_L. Black solid (dotted) lines: $n_\mu(\boldsymbol{p}) = \mu\sigma T/|\boldsymbol{p}-\boldsymbol{p}_0|$. (c) Filled circles: W_b versus Φ. (d) Filled circles: $W_b^{1/2}$ versus $I^{1/2}$ ($\tau_L = 7$ fs). Solid line: a linear fit to the data.

4.3. XBP statistical properties

The S-like lines in Fig. 5(a) plot the energy-integrated and normalized spectra,

$$q(W) = \int_{W_a}^{W} \mathrm{d}W' n(W')/Y_X, \tag{16}$$

calculated with $\tau_L = 7$ fs, $\Phi = 0°$, and different I, where

$$Y_X = \int_{W_a}^{W_b} n(W')\mathrm{d}W', \tag{17}$$

is the total XBP production. Because $n(W)$ has structures due to interference, we define an observable value Q,

$$\begin{aligned} Q &\equiv \int_{W_0}^{W_b} \mathrm{d}W \int_{W}^{W_b} q(W')\mathrm{d}W' \\ &= \int_{W_0}^{W_b} \mathrm{d}W \int_{W}^{W_b} \mathrm{d}W' n(W')/Y_X. \end{aligned} \tag{18}$$

Q is a double integration. Here, $n(W')$ is integrated from W ($> W_0$) to W_b because the low energy portion of $n(W)$ ($W < W_0$) may be polluted by ATI and XBP with lower values of I_p. Calculations show that Y_X remains unchanged as I (or τ_L, Φ) varies [see the filled circles in Figs. 6(c) and 6(d)], and Q depends on I and τ_L but not on Φ. The calculated results ensure that Q varies for different I. The filled circles in Fig. 5(b) show Q values calculated with different I ($\tau_L = 7$ fs). The solid line is a parabola fit of the data corresponding to I versus Q, or equivalently, $Q = b_1(I+b_2)^{1/2}+b_3$, where b_1, b_2, b_3 are fit values [shown in Fig. 6(b)].

The volume integration of the spectral contributions from the lower intensities of the iso-intensity shells [see Fig. 1(b)] gives a total Q signal:

$$Q_{\mathrm{XBP}}(I) = 2\pi \int_0^\infty \mathrm{d}r \cdot r[b_1(I\mathrm{e}^{-4\ln 2\cdot r^2/\tau_R^2}+b_2)^{1/2}+b_3]. \tag{19}$$

Figure 6(a) shows the energy-integrated and normalized PES $q(W)$ (S-like lines), calculated with $\Phi = 0°$, $I = 5\times10^{14}$ W/cm^2, and different τ_L ranging from 5 to 25 fs. The filled circles in Fig. 6(b) plot Q values that have been calculated with different τ_L and the specified single intensity $I = 5\times10^{14}$ W/cm^2. The solid line is linearly fitted from Q data. With the expression of $Q_{\mathrm{XBP}}(I)$ [Eq. (19)], this linear line for single laser intensity I can be modified to another linear line $Q_{\mathrm{XBP}}(\tau_L) = c(I)\tau_L$ for volume integration, where $c(I)$ depends on I. A calculated (or measured) line $Q_{\mathrm{BXP}}(\tau_L)$, which has been calibrated with known τ_L pulses, can be used for the τ_L measurement. Unlike Y_L in the ATI case, $Q(I)$ [$Q(\tau_L)$] increases to 34.7 eV (140 eV) when I (τ_L) changes from $I = 10^{12}$ W/cm^2 to 2×10^{15} W/cm^2 ($\tau_L = 5$ fs to 60 fs). A comparison between $Y_{L>15\ \mathrm{eV}} = -0.0035+0.0039\tau_L$ [Fig. 2(c)] and $Q = 0.2617+2.3285\tau_L$ [in units of eV, Fig. 6(b)] indicates that Q (XBP signal) is more sensitive to τ_L than $Y_{L>15\ \mathrm{eV}}$ (ATI signal). Calculations with different I, τ_L, and Φ give similar results, as shown in Figs. 6(a) and 6(b).

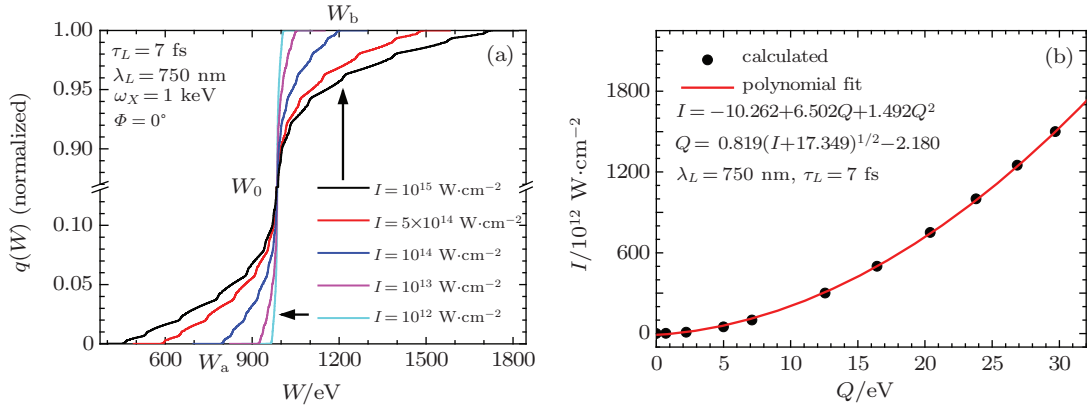


Fig. 5. (color online) XBP statistical properties. (a) S-like lines: the energy-integrated and normalized photoelectron energy spectra, $q(W) = \int_{W_a}^{W} \mathrm{d}W' n(W')/Y_X$, calculated with $\tau_L = 7$ fs and different I, where $Y_X = \int_{W_a}^{W_b} n(W')\mathrm{d}W'$. (b) I versus Q, where $Q = \int_{W_0}^{W_b} \mathrm{d}W \int_{W}^{W_b} \mathrm{d}W' n(W')/Y_X$.

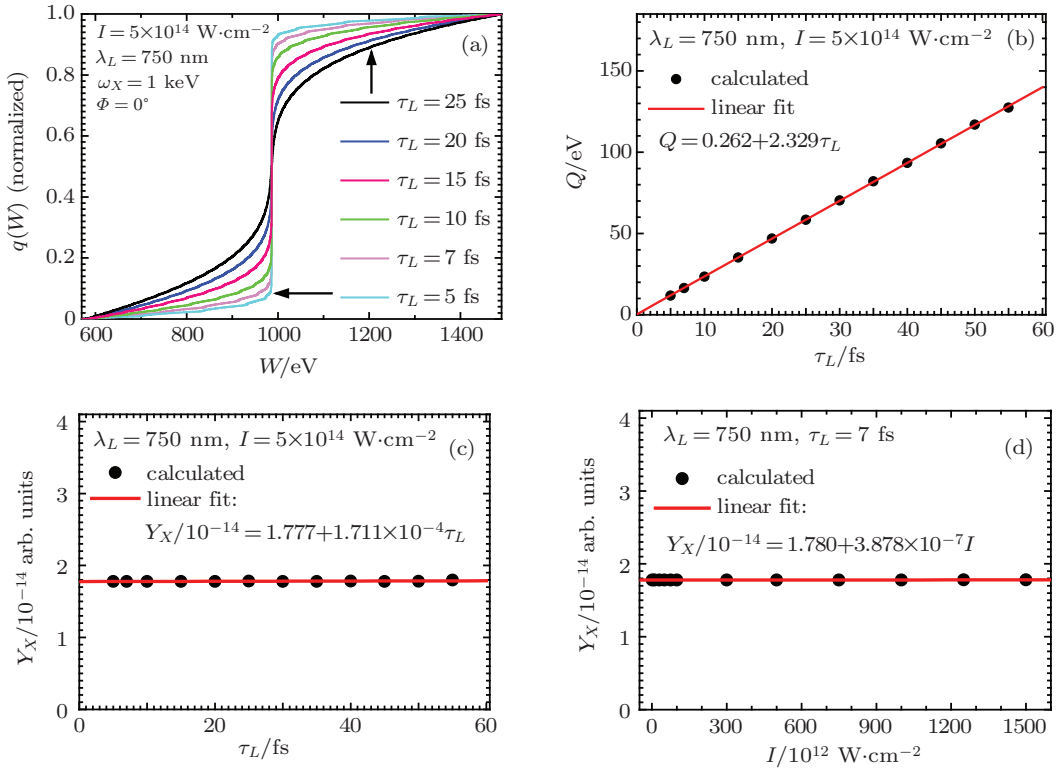


Fig. 6. (color online) XBP statistical properties (color online). (a) S-like lines: the energy-integrated and normalized photoelectron energy spectra $q(W)$, calculated with $I = 5\times10^{14}$ W/cm^2 and different τ_L. (b) Filled circles: Q versus τ_L. Solid line: a linear fit of the data. (c) Filled circles: Y_X versus τ_L ($I = 5\times10^{14}$ W/cm^2). Solid line: a linear fit of the data. (d) Filled circles: Y_X versus I ($\tau_L = 7$ fs). Solid line: a linear fit of the data.

Figures 6(c) and 6(d) show the data corresponding to the total XBP productions Y_X calculated with different laser pulse durations τ_L and intensities I, respectively. The solid lines are linearly fitted from the data. We see that Y_X remains almost unchanged as τ_L or I varies in broad ranges. Calculations with different CEP Φ values give similar results as those shown in Figs. 6(c) and 6(d).

5. Conclusion

The proposed methods open a new window for observing and using ultrahigh lasers. The laser pulse in XBP acts as an electron energy modulator. The total photoionization yield Y_X linearly depends on the X-ray intensity I_X. The double integration Q is sensitive to the laser intensity I and pulse duration τ_L but does not change as the CEP Φ changes. The *in-situ* measurement of an intense laser pulse can be achieved with high accuracy, at broad ranges (up to many intensity orders), and with a simplified algorithm to extract the pulse information from a measured PES. I and Φ can be determined from the PES cut-off energy W_b, τ_L can be determined from a calibrated line $Q_{\mathrm{XBP}}(\tau_L) = c(I)\tau_L$, and time t and $F(t)$ can be determined from relatively high peak positions of a measured PES. Although the calculations are performed with $I < 10^{16}$ W/cm^2, the method can work with higher laser in-

tensities ($I > 10^{16}$ W/cm^2) by using high energy X-rays and highly charged inert gases. The proposed measurement configuration and physical results have referential meanings for further research with laser intensities less than 10^{12} W/cm^2 and higher than 10^{18} W/cm^2 where Lorentz force plays an important role on the photoelectron motion.

References

[1] Krauss G, Lohss S, Hanke T, Sell A, Eggert S, Huber R and Leitenstorfer A 2010 *Nat. Photon.* **4** 33

[2] Yanovsky V, Chvykov V, Kalinchenko G, Rousseau P, Planchon T, Matsuoka T, Maksimchuk A, Nees J, Cheriaux G, Mourou G and Krushelnick K 2008 *Opt. Express* **16** 2109

[3] Wiehle R, Witzel B and Helm H 2003 *Phys. Rev. A* **67** 063405

[4] Goulielmakis E, Schultze M, Hofstetter M, Yakovlev V S, Gagnon J, Uiberacker M, Aquila A L, Gullikson E M, Attwood D T, Kienberger R, Krausz F and Kleineberg U 2008 *Science* **320** 1614

[5] Bula C, McDonald K T, Prebys E J; Bamber C, Boege S, Kotseroglou T, Melissinos A C, Meyerhofer D D, Ragg W; Burke D L, Field R C, Horton-Smith G, Odian A C, Spencer J E, Walz D; Berridge S C, Bugg W M, Shmakov K and Weidemann A W 1996 *Phys. Rev. Lett.* **76** 3116

[6] Mourou G and Tajima T 2011 *Science* **331** 41

[7] L'Huillier A, Lompre L A, Mainfray G and Manus C 1983 *J. Phys. B* **16** 1363

[8] Link A, Chowdhury E A, Morrison J T, Ovchinnikov V M, Offermann D, Woerkom L V, Freeman R R, Pasley J, Shipton E, Beg F, Rambo P, Schwarz J, Geissel M, Edens A and Porter J L 2006 *Rev. Sci. Instrum.* **77** 10E723

[9] Akahane Y, Ma J L, Fukuda Y, Aoyoma M, Kiriyama H, Sheldakova J V, Kudryashov A V and Yamakawa K 2006 *Rev. Sci. Instrum.* **77** 023102

[10] Alnaser A S, Tong X M, Osipov T, Voss S, Maharjan C M, Shan B, Chang Z and Cocke C L 2004 *Phys. Rev. A* **70** 023413

[11] Smeenk C, Salvail J Z, Arissian L, Corkum P B, Hebeisen C T and Staudte A 2011 *Opt. Express* **19** 9336

[12] Scrinzi A, Geissler M and Brabec T 2001 *Phys. Rev. Lett.* **86** 412

[13] Itatani J, Quéré F, Yudin G L, Ivanov M Y, Krausz F and Corkum P B 2002 *Phys. Rev. Lett.* **88** 173903

[14] Bandrauk A D, Chelkowski S and Shon N H 2002 *Phys. Rev. Lett.* **89** 283903

[15] Quéré F, Itatani J, Yudin G L and Corkum P B 2003 *Phys. Rev. Lett.* **90** 073902

[16] Ge Y C 2006 *Phys. Rev. A* **74** 015803

[17] Ge Y C 2008 *Phys. Rev. A* **77** 033851

[18] Ge Y C and He H P 2011 *Phys. Rev. A* **84** 023804

[19] Ge Y C 2008 *Chin. Phys. B* **17** 2072

[20] Ge Y C 2008 *Chin. Phys. B* **17** 4492

[21] Ge Y C 2009 *Chin. Phys. B* **18** 1473

[22] Ge Y C and He H P 2010 *Chin. Phys. B* **19** 103302

[23] Drescher M, Hentschel M, Kienberger R, Tempea G, Spielmann C, Reider G A, Corkum P B and Krausz F 2001 *Science* **291** 1923

[24] Hentschel M, Kienberger R, Spielmann C, Reider G A, Milosevic N, Brabec T, Corkum P B, Heinzmann U, Drescher M and Krausz F 2001 *Nature* **414** 509

[25] Drescher M, Hentschel M, Kienberger R, Uiberacker M, Yakovlev V, Scrinzi A, Westerwalbesloh T, Kleineberg U, Heinzmann U and Krausz F 2002 *Nature* **419** 803

[26] Kienberger R, Goulielmakies E, Uiberacker M, Baltuska A, Yakovlev V, Bammer F, Scrinzi A, Westerwalbesloh T, Kleineberg U, Heinzmann U, Drescher M and Krausz F 2004 *Nature* **427** 817

[27] Goulielmakis E, Uiberacker M, Kienberger R, Baltuska A, Yakovlev V, Scrinzi A, Westerwalbesloh T, Kleineberg U, Heinzmann U, Drescher M and Krausz F 2004 *Science* **305** 1267

[28] Lewenstein M, Balcou P, Ivanov M Y, L'Huillier A and Corkum P B 1994 *Phys. Rev. A* **49** 2117